PAPER

Check for updates

Construction of a La-ZnIn₂S₄/MIL-125(Ti) heterojunction for highly efficient photocatalytic degradation of aflatoxin B₁

Xiaobing Yang, [ID] [abc] Junjie Pan,[c] Bingcong Xing,[d] Wenjie Lei,[b] Yingchun Fu [ID] *[a] and Kejun Cheng*[cd]

Nowadays, aflatoxin B₁ (AFB₁) contamination is considered as one of the most common food safety issues for humans and animals. As one of the most advanced oxidation techniques, photocatalytic degradation can break down organic contaminants into nontoxic and harmless materials efficiently. In this paper, we explored the degradation efficiency of AFB₁ by ZnIn₂S₄. To promote the photocatalytic degradation efficiency of AFB₁, ZnIn₂S₄ was coupled with MIL-125(Ti) and then doped with La [this hybrid is denoted as La-ZnIn₂S₄/MIL-125(Ti)] to effectively convert it *via* photocatalytic generation of superoxide radicals ($\bullet O_2^-$ and $\bullet OH$) and achieve much enhanced photocatalytic performance, which is demonstrated by degrading 97.6% of AFB₁. According to the transient photocurrent responses, the doping of La and coupling with MIL-125(Ti) can highly improve the efficient separation of the photoinduced electron–hole pairs on ZnIn₂S₄, leading to the effective conversion of OH⁻ and O₂ into $\bullet O_2^-$ and $\bullet OH$, respectively, during the photodegradation process. This strategy of coupling with MOFs and doping with rare earth elements provides a facile and efficient method for degrading food pollutants produced by aflatoxins.

Introduction

In recent years, consumers and producers have drawn much attention to food safety. One of the most common food safety issues comes from mycotoxin contamination, which exists in a variety of products ranging from food to feed.[1] Aflatoxins, as one of the most toxic and carcinogenic mycotoxins, are secondary fungal metabolites of *Aspergillus flavus* and *Aspergillus parasiticus*, especially aflatoxin B₁ (AFB₁), which has been listed as a type one carcinogen by the International Agency for Research on Cancer and probably causes serious effects in humans and animals, such as bleeding, chronic toxicity, carcinoma and immunosuppression even when exposed to an extremely low level.[2–4] Aflatoxins have high chemical and thermal stability. It is difficult to destroy them and still they possess toxic activity even after being treated with high temperatures.[5]

Aflatoxins not only are one of the important threats to animal and human health, but also cause great economic losses all over the world.

To reduce, eliminate, and prevent the risks in animals and humans, numerous methods have been utilized to remove or/ and degrade aflatoxins. For example, Xu and his co-workers developed polydopamine-modified magnetic multi-wall carbon nanotubes for the adsorption and removal of aflatoxins and ochratoxins from vegetable oils.[6] Xing and his team adopted roasting with a lemon juice and/or citric acid method to remove aflatoxin B₁.[7] Xing and his co-workers used a Spin-X centrifuge system to investigate the AFB₁ degradation of atoxigenic GZ15 and JZ2.[8] Although these strategies can remove or/and reduce aflatoxins to some degree, they are restricted by some factors. For example, the adsorption of aflatoxins can bring secondary contamination, the chemical method will leave some chemicals in the environment, and the gene method is restricted by the technical requirements.[9,10] Moreover, with the growing demands for food safety and environmental protection, it is vital to develop newer and greener technologies that can break aflatoxins into nontoxic and harmless materials more efficiently, environment-friendly, and affordably.

As one of the most advanced oxidation techniques, photocatalysis technology can degrade organic contaminants with many benefits, such as efficiency, eco-friendliness, no secondary

[a] College of Biosystems Engineering and Food Science, Zhejiang University, Hangzhou 310058, Zhejiang Province, China. E-mail: ycfu@zju.edu.cn

[b] Fujian Provincial Key Laboratory of Eco-Industrial Green Technology, Wuyi University, Wuyishan 354300, Fujian Province, China

[c] Chemical Biology Center, Lishui Institute of Agriculture and Forestry Sciences, Lishui 323000, Zhejiang Province, China. E-mail: chengkejun@gmail.com

[d] Zhejiang Province Key Laboratory of Resources Protection and Innovation of Traditional Chinese Medicine, Zhejiang A&F University, Hangzhou 311300, Zhejiang Province, China

pollution, easy operation, and low cost.[11] Photocatalysts, for example, $ZnIn_2S_4$, can break down the organic contaminants into non-toxic and harmless materials under UV or/and visible light irradiation. Hence, this technology holds great promise for detoxifying aflatoxins. However, the photocatalytic degradation efficiency of photocatalysts suffers from the rapid combination of the photoexcited electron–hole pairs.[12] Some measures need to be taken to improve its photocatalytic activity. In this paper, we introduced a novel La doped $ZnIn_2S_4$ coupled with MIL-125(Ti) to form a unique composite structure of La-$ZnIn_2S_4$/MIL-125(Ti). It showed much improved photocatalytic decomposition of AFB_1 with UV illumination. The influences of MIL-125(Ti) coupling and La doping on the AFB_1 degradation efficiency of $ZnIn_2S_4$ were investigated, and the degradation mechanism of AFB_1 by La-$ZnIn_2S_4$/MIL-125(Ti) was also systematically explored in detail.

Experimental

Materials

N,N-Dimethylformamide (DMF), ethanol, 1,4-dicarboxybenzene ($C_8H_6O_4$), methanol, and tetrabutyl titanate ($C_{16}H_{36}O_4Ti$) were bought from Sinopharm Chemical Reagent (Shanghai, China). Thioacetamide (CH_3CSNH_2), lanthanum nitrate [$La(NO_3)_2$], and aflatoxin B_1 (AFB_1) were obtained from Aladdin (Shanghai, China). Indium chloride ($InCl_3$) and zinc chloride ($ZnCl_2$) were supplied by Alfa Aesar (Shanghai, China). The chemicals were used directly since they were of analytical grade.

Synthesis of the La-$ZnIn_2S_4$/MIL-125(Ti) catalyst

The MOF material of MIL-125(Ti) was synthesized using a method adopted from the previously published solvothermal synthesis.[13] Typically, 5 g of $C_8H_6O_4$ and 30 mL of ethanol were dissolved in 270 mL of DMF, by stirring at room temperature for 0.5 h. Then, 2.6 mL of $C_{16}H_{36}O_4Ti$ was mixed with the $C_8H_6O_4$ solution followed by stirring for 15 min before being moved into a PTFE vessel (500 mL). The vessel was sealed and the solution was reacted for 24 h at 150 °C. White precipitates were collected by centrifugation at room temperature. The obtained MIL-125(Ti) solid sample was purified by washing with ethanol and DMF three times, and then dried at 80 °C.

The La-$ZnIn_2S_4$/MIL-125(Ti) composite was synthesized using a modified hydrothermal process. 0.05 g of $La(NO_3)_2$, 0.677 g of $InCl_3$, 0.455 g of CH_3CSNH_2, and 0.206 g of $ZnCl_2$ were added to DMF (100 mL) followed by stirring at room temperature for 0.5 h until all the added chemical reagents were fully dissolved before adding 0.9 g of the synthesized MIL-125(Ti) crystallized particles. The mixture was stirred for 10 min before sealing in a 200 mL PTFE container. The sample was heated to 180 °C for 10 h. After reaction, a yellow powder was obtained by centrifugation, washed with ethanol three times, and dried at 80 °C. For comparison, $ZnIn_2S_4$ and $ZnIn_2S_4$/MIL-125(Ti) were fabricated using the same process without adding $La(NO_3)_2$. The synthesis procedure is illustrated in Fig. 1.

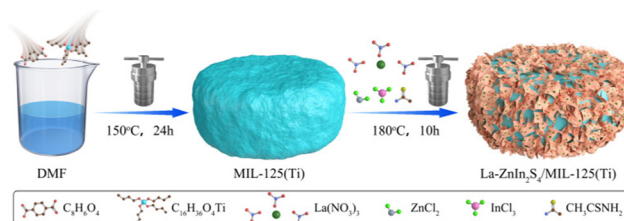Fig. 1 The procedure for La-$ZnIn_2S_4$/MIL-125(Ti) synthesis.

Characterization

The crystal structures were studied using a powder X-ray diffractometer (PXRD, D8 Advance, Bruker) using Cu Kα X-ray (λ = 1.54168 Å). The morphology of all samples was investigated by scanning electron microscopy (SEM, S4800, Hitachi, Japan). Infrared vibrational spectra were obtained using a Fourier transform infrared (FT-IR) spectrophotometer (Vector22, Bruker). Brunauer–Emmett–Teller (BET) specific surface areas were measured using the N_2 adsorption–desorption isotherms at 77 K obtained using a BET analyzer (ASAP 2000, Micromeritics). The light absorption was recorded on a UV-Vis spectrometer (UV2450) equipped with diffuse reflectance (DRS) attachments. The photoelectrochemical properties, including the electrochemical impedance spectrum (EIS), were investigated on a CHI760E workstation. A scanning transmission electron microscope (TEM, JEM-2100HR, Jeol) was used to study the structure of the samples. Surface element composition and associated oxidation states were measured using an X-ray photoelectron spectrometer (XPS, Escalab 250Xi) equipped with Al Kα emission. Radical intermediates were identified by electron spin resonance (ESR) spectroscopy (A-300, Bruker) using spin trap 5,5-dimethyl-1-pyrroline N-oxide (DMPO) to identify the free radicals.

Evaluation of photocatalytic activity

The photocatalytic degradation measurements were carried out in a photochemical reactor (SH-EJE-A, Shanghai EHE Instrument, China). A mercury lamp (500 W) was adopted as the UV light source. During the degradation experiment, the photocatalyst (0.05 g) was dispersed in a freshly prepared AFB_1 aqueous solution (100 mL, 5 ppm). To eliminate the adsorption, the adsorption equilibrium was reached by stirring the suspension solution for 30 min without light. During irradiation, a small amount of solution was sampled from the photochemical vessel at certain duration. The solid photocatalyst was removed by centrifugation. The concentrations of AFB_1 solution were detected using a UV-vis spectrophotometer. The stability of the photocatalyst was also evaluated by repeating the photodegradation for five recycles. At the end of each degradation reaction, the photocatalyst was collected, washed with water, and dried at 80 °C before the next degradation reaction.

Results and discussion

Fig. 2 shows the XRD patterns and the FT-IR spectrum of La-$ZnIn_2S_4$/MIL-125(Ti) is compared with that of the $ZnIn_2S_4$/MIL-125(Ti)
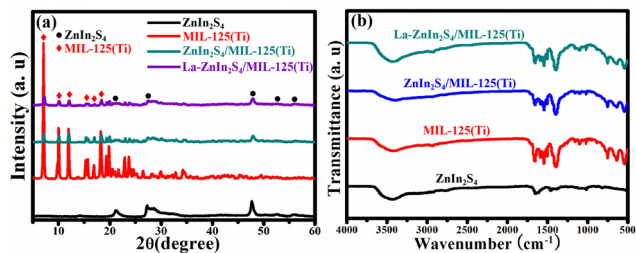
Fig. 2 (a) XRD patterns and (b) FT-IR spectra of $ZnIn_2S_4$, MIL-125(Ti), $ZnIn_2S_4$/MIL-125(Ti) and La-$ZnIn_2S_4$/MIL-125(Ti).

composite, together with those of the $ZnIn_2S_4$ and MIL-125(Ti) precursors. As shown in Fig. 2a, $ZnIn_2S_4$ exhibits three main peaks at 21.2°, 27.5°, and 47.7°, which are ascribed to the (006), (102), and (110) crystal planes of $ZnIn_2S_4$ (JCPDS No. 65-2023), respectively.[14] MIL-125(Ti) exhibits six characteristic peaks at 7.10°, 9.86°, 11.99°, 15.35°, 16.89°, and 18.22°, indicating its formation.[15,16] With the coupling of MIL-125(Ti) with $ZnIn_2S_4$, it shows the representative peaks of both MIL-125(Ti) and $ZnIn_2S_4$. Interestingly, the intensity corresponding to MIL-125(Ti) is not as strong as that without the coupling of $ZnIn_2S_4$. Thus, the coupling with $ZnIn_2S_4$ caused the structure and morphology changes of MIL-125(Ti). Other researchers have reported similar changes in the XRD patterns of the $ZnIn_2S_4$/MOF composites in the literature.[17,18] Fig. 2d shows the XRD spectrum of the La-$ZnIn_2S_4$/MIL-125(Ti) composite, which is almost the same as that of the composite without La coupling, indicating that the doping of La has no effects on the crystal structure.

FT-IR spectra were recorded to study the functional groups and chemical bonding in different samples. As shown in Fig. 2b, all samples have a broad peak centered at 3470 cm^{-1} and two distinct absorption bands at 1610 and 1397 cm^{-1} from the absorbed water molecules.[19] $ZnIn_2S_4$ exhibits similar characteristic peaks to the previous reports.[20] The broad absorption band between 400 and 800 cm^{-1} for MIL-125(Ti) is assigned to the O–Ti–O vibration. Two clear absorptions at 1406 and 1653 cm^{-1} are linked to the O–C–O vibrational stretching.[21] The C=C stretching in the aromatic ring peak is at 1510 cm^{-1}.[22] The feature at 1705 cm^{-1} is typical for a pristine BDC.[23] $ZnIn_2S_4$/MIL-125(Ti) shows almost identical absorption bands to the MOF. However, a slight peak shift for the characteristic O–Ti–O peak was observed for $ZnIn_2S_4$/MIL-125(Ti), suggesting the chemical coupling between the MOF and $ZnIn_2S_4$. La-$ZnIn_2S_4$/MIL-125(Ti) has an almost identical IR spectrum to ZnIn2S4/MIL-125(Ti), inferring that the doping of La does not affect the molecular structure and the chemical bonding of $ZnIn_2S_4$/MIL-125(Ti).

The SEM images were used to analyze the morphologies of the precursors and composites. As shown in Fig. 3a, the MIL-125(Ti) MOF exhibited a plate-like crystallized morphology with a smooth surface, and its particle size is 350–600 nm. Fig. 3b shows the SEM image of $ZnIn_2S_4$, which shows a flower-like microsphere morphology with an average diameter of about 2 μm and the flower-like microsphere is assembled by
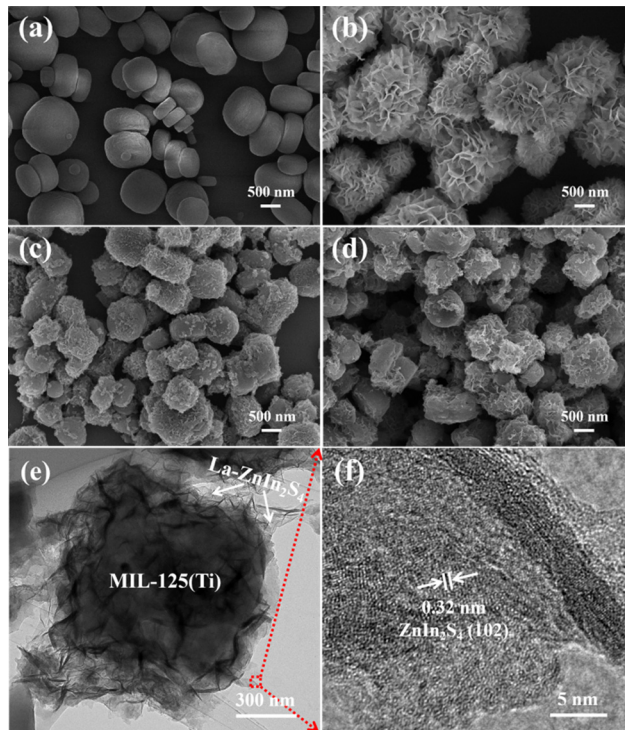

Fig. 3 SEM images of (a) MIL-125(Ti), (b) $ZnIn_2S_4$, (c) $ZnIn_2S_4$/MIL-125(Ti), and (d) La-$ZnIn_2S_4$/MIL-125(Ti), and (e) TEM and (f) HRTEM images of La-$ZnIn_2S_4$/MIL-125(Ti).

numerous cross-linked nanosheets. As shown in the SEM image of $ZnIn_2S_4$/MIL-125(Ti) in Fig. 3c, many $ZnIn_2S_4$ nanosheets were attached on the surface facets of the MOF. According to Yuan's report, coating $ZnIn_2S_4$ nanosheets on MOFs can weaken the characteristic peaks,[24] which is in agreement with the XRD patterns. No significant change of the morphology was observed in La-$ZnIn_2S_4$/MIL-125(Ti) (Fig. 3d) with respect to $ZnIn_2S_4$/MIL-125(Ti) (Fig. 3c). Hence, the structure of the $ZnIn_2S_4$/MIL-125(Ti) composite did not change after the La doping. TEM and HRTEM images were used to investigate further the morphology and internal structure of La-$ZnIn_2S_4$/MIL-125(Ti). As shown in Fig. 3b, $ZnIn_2S_4$ exhibits a flower-like spherical morphology with numerous aggregated nanosheets. However, when $ZnIn_2S_4$ is coupled with MIL-125(Ti) (Fig. 3e), its cross-linked nanosheets are disconnected and evenly distributed on the crystal planes of MIL-125(Ti). The high-magnification image in Fig. 3f shows the surface unfolded nanosheets. The high-magnification image of these unfolded nanosheets displays a clear lattice fringe of 0.32 nm, assigned to the $ZnIn_2S_4$ (102) crystal plane,[25] indicating the successful coupling of $ZnIn_2S_4$ on the MIL-125(Ti) crystal surfaces. There are no signals for the La element in the unfolded nanosheets of $ZnIn_2S_4$, possibly due to low content.

Fig. 4 shows the BET measurement results, summarized in Table 1, with the specific surface area (S_{BET}, m^2 g^{-1}), total volume of the pore (V_{total}, cm^3 g^{-1}), total volume of the micropore (V_{micro}, cm^3 g^{-1}), and pore diameter (D, nm). As displayed
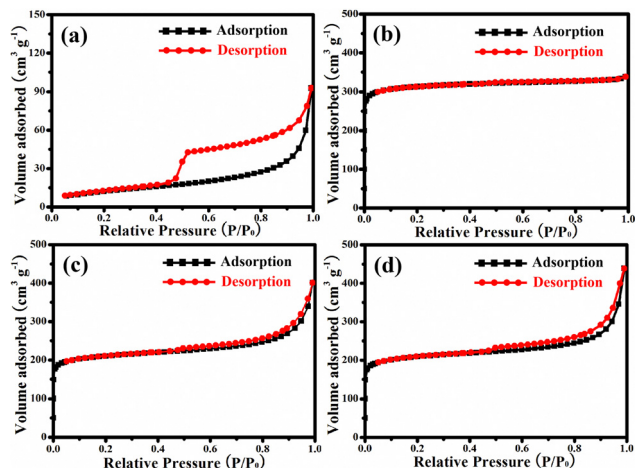
Fig. 4 N_2 adsorption–desorption isotherms of (a) $ZnIn_2S_4$, (b) MIL-125(Ti), (c) $ZnIn_2S_4$/MIL-125(Ti) and (d) La-$ZnIn_2S_4$/MIL-125(Ti).

Table 1 Textural properties of all samples

Sample	S_{BET}[a]	V_{total}[b]	V_{micro}[c]	D[d]
$ZnIn_2S_4$	45.14	0.144	0.004	6.49
MIL-125(Ti)	959.93	0.512	0.430	2.13
$ZnIn_2S_4$/MIL-125(Ti)	653.05	0.469	0.258	2.87
La-$ZnIn_2S_4$/MIL-125(Ti)	650.65	0.473	0.253	2.91

[a] Specific surface area ($m^2\ g^{-1}$). [b] Total pore volume ($cm^3\ g^{-1}$). [c] T-plot micropore volume ($cm^3\ g^{-1}$). [d] Average pore diameter (nm).

in Fig. 4a, $ZnIn_2S_4$ shows the type-IV isotherm with a distinct H3 hysteresis loop in the range from 0.47 to 1.00 (P/P_0), confirming its mesoporous structure.[26] The corresponding BET surface area is 45.14 $m^2\ g^{-1}$. MIL-125(Ti) showed initial high adsorption of N_2 at a relative pressure of 0–0.1 (P/P_0), which belongs to the type-I isotherm and indicates its microporous structure.[27] Fig. 4c shows the adsorption–desorption curves of $ZnIn_2S_4$/MIL-125(Ti). It shows a high uptake at a relative pressure of 0–0.1 (P/P_0) and the H3 hysteresis loop in the range from 0.47 to 1.00 (P/P_0), illustrating that $ZnIn_2S_4$/MIL-125(Ti) has both the microporous and mesoporous structures. La-$ZnIn_2S_4$/MIL-125(Ti) (Fig. 4d) has a similar adsorption–desorption behavior to $ZnIn_2S_4$/MIL-125(Ti). The S_{BET} of La-$ZnIn_2S_4$/MIL-125(Ti) is 650.65 $m^2\ g^{-1}$ while the corresponding D is 2.91 nm, as shown in Table 1, which are almost the same as those of $ZnIn_2S_4$/MIL-125(Ti), confirming that the doping of La does not change the textural properties of $ZnIn_2S_4$/MIL-125(Ti).

The optical absorption of the powder was analyzed using a UV-Vis DRS spectrophotometer. The following equation can be used to calculate the band gap energy (E_g): $E_g = 1240/\lambda$ (λ is the absorption edge).[28] MIL-125(Ti) displays a strong absorption between 300 and 350 nm, as shown in Fig. 5, which is assigned to the intrinsic band gap. $ZnIn_2S_4$ shows a visible light absorption edge near 494 nm with the corresponding band gap energy of 2.51 eV. When $ZnIn_2S_4$ is combined with MIL-125(Ti), its absorption edge is slightly broadened to 498 nm ($E_g = 2.49$ eV).
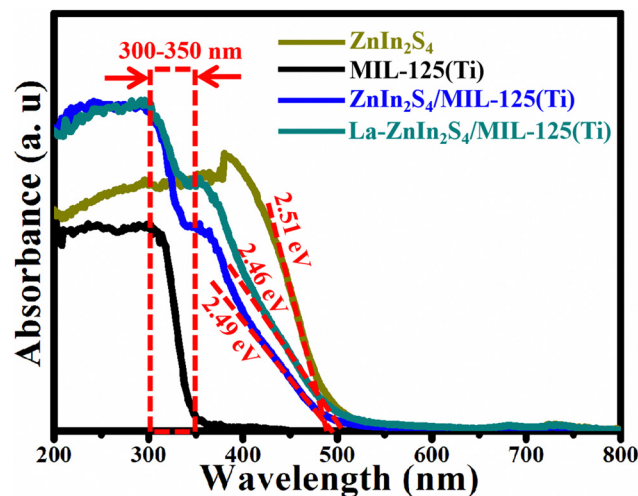

Fig. 5 The UV-vis absorbance spectra of $ZnIn_2S_4$, MIL-125(Ti), $ZnIn_2S_4$/MIL-125(Ti) and La-$ZnIn_2S_4$/MIL-125(Ti).

More interestingly, the doping of La on $ZnIn_2S_4$/MIL-125(Ti) can further broaden its absorption edge from 498 to 504 nm ($E_g = 2.46$ eV). According to Table 1, MIL-125(Ti) recombining on $ZnIn_2S_4$ can improve its BET surface area. The doping of La and MIL-125(Ti) recombining on $ZnIn_2S_4$ can raise its adsorption capacity of contaminants and promote it to excite more photoexcited electrons and holes during the photocatalysis.

Generally, the excellent photoactivity of a photocatalyst is associated with the good charge separation efficiency. The photoelectrochemical technique was used to analyze the interfacial charge separation of photocatalysts. Fig. 6a shows the photocurrent response with the light on and off from different photoanodes under UV illumination for seven on–off cycles. With UV light, the photocurrents from the samples without La doping decreased rapidly to zero, attributed to the fast combination of photoinduced electron–hole pairs. The photocurrent density of $ZnIn_2S_4$/MIL-125(Ti) (1.48 $\mu A\ cm^{-2}$) is higher than
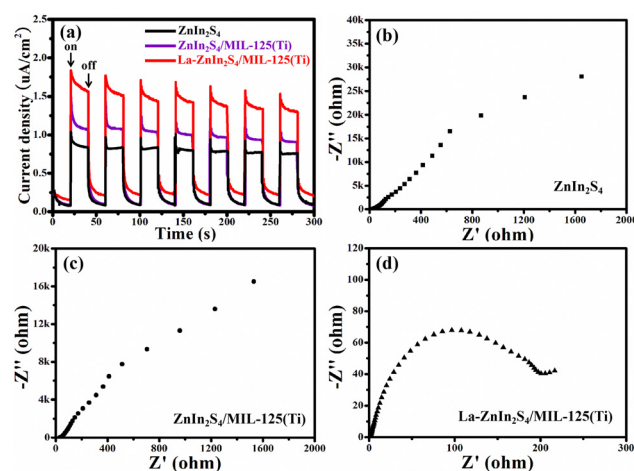

Fig. 6 (a) Transient photocurrent responses and electrochemical impedance spectra of (b) $ZnIn_2S_4$, (c) $ZnIn_2S_4$/MIL-125(Ti) and (d) La-$ZnIn_2S_4$/MIL-125(Ti).

that of $ZnIn_2S_4$ (1.02 µA cm^{-2}), indicating that the coupling of MIL-125(Ti) enhanced the photoactivity of $ZnIn_2S_4$. The photocurrent of La-$ZnIn_2S_4$/MIL-125(Ti) is 1.87 µA cm^{-2} and La-$ZnIn_2S_4$/MIL-125(Ti) exhibits the highest photocurrent density. Noticeably, when the UV light is switched on, the photocurrent of La-$ZnIn_2S_4$/MIL-125(Ti) decreases to a certain value and then slows down to zero, confirming that La-$ZnIn_2S_4$/MIL-125(Ti) has the best charge separation efficiency. The results verify that the doping of La and the coupling with MIL-125(Ti) can effectively enhance the efficiency of charge separation due to the transfer of photoinduced electrons from $ZnIn_2S_4$ to La and MIL-125(Ti). To explore the enhancement mechanism, the EIS measurements were carried out for different photoanodes. The semicircle size in the Nyquist plot for La-$ZnIn_2S_4$/MIL-125(Ti) is the smallest among all the samples, representing the lowest interface resistance of La-$ZnIn_2S_4$/MIL-125(Ti). Thus, La doping and MIL-125(Ti) coupling have improved the charge separation in $ZnIn_2S_4$ in the photoexcitation process.

The elemental composition and the chemical state of La-$ZnIn_2S_4$/MIL-125(Ti) were established by XPS. Fig. 7a shows the XPS survey spectrum of La-$ZnIn_2S_4$/MIL-125(Ti), in which the elements La, Zn, In, S, Ti, Ti, N, and O with sharp photoelectron peaks can be identified. However, the N intensity is relatively low, indicating low content of N, which may have come from the adsorbed N_2. Fig. 7b shows the high-resolution La 3d XPS spectrum, which depicts four peaks with their binding energies centered at 834.7, 838.1, 852.5, and 854.9 eV, revealing the existence of La^{3+} ions.[29] Compared with the standard XPS peaks

of La 3d in pure La_2O_3, the La 3d spectrum of La-$ZnIn_2S_4$/MIL-125(Ti) shows a slight shift to a lower binding energy direction, indicating that La^{3+} ions are dissolved into the $ZnIn_2S_4$ lattice.[30] The Zn 2p high resolution XPS spectrum in Fig. 7c shows two distinctive signals at 1021.8 and 1044.9 eV, associated with the spin orbit coupling. The high resolution In 3d XPS spectrum in Fig. 7d shows the In spin orbit coupling signals at 444.7 and 451.5 eV. As for the S 2p spectrum (Fig. 7e), its $2p_{3/2}$ and $2p_{1/2}$ signals were observed at 161.4 and 162.7 eV. As shown in Fig. 7f the C 1s spectrum has four components. The two peaks at lower energies of 284.4 and 285.1 eV are assigned to the C=C and C–C bonds, while the other two peaks at higher energies of 286.2 and 288.9 eV are associated with the carbon atoms bonded with oxygen in the C–O, and C=O structures in BDC. Our XPS results verify the successful doping of La^{3+} in the La-$ZnIn_2S_4$/MIL-125(Ti) composite.

The experiment for the degradation of AFB_1 solution by photocatalysts was performed under UV light irradiation. Before the photocatalytic degradation, the photocatalysts were dispersed in the AFB_1 solution by stirring for 30 min without light to achieve the adsorption equilibrium. Then, the solution was exposed to UV light. As shown in Fig. 8a, the concentration of AFB_1 exhibits a slight decrease (the black line) without adding the catalyst under UV light irradiation, indicating the negligible self-degradation of AFB_1. After 28 min of illumination, the photodegradation efficiencies of MIL-125(Ti) (51.4%), $ZnIn_2S_4$ (85.5%), $ZnIn_2S_4$/MIL-125(Ti) (89.5%), and La-$ZnIn_2S_4$/MIL-125(Ti) (97.6%) were achieved. The best photocatalytic performance was achieved by La-$ZnIn_2S_4$/MIL-125(Ti). Besides that, stability is also very important for the photocatalyst.

The experimental cycling runs of La-$ZnIn_2S_4$/MIL-125(Ti) are used to evaluate its stability. As displayed in Fig. 8b, after five times repetition, the degradation efficiency of La-$ZnIn_2S_4$/MIL-125(Ti) reduces by 3.1%, without changes in XRD patterns (Fig. 8c). Hence La-$ZnIn_2S_4$/MIL-125(Ti) offers excellent photocatalytic performance stability, in addition to its good structural stability.

The photoinduced reactive species (RS) are essential as the active intermediates produced during photocatalysis. ESR spectroscopy was used to examine the generated RS by La-$ZnIn_2S_4$/MIL-125(Ti) under UV light irradiation with DMPO as the radical trapper. As shown in Fig. 9, no ESR peak was visible without UV illumination. However, the four-line characteristic peak of DMPO-$^{\bullet}O_2^{-}$ and the 1:1:1 triplet characteristic peak of DMPO-$^{\bullet}$OH are detected under UV light irradiation for 5 min,

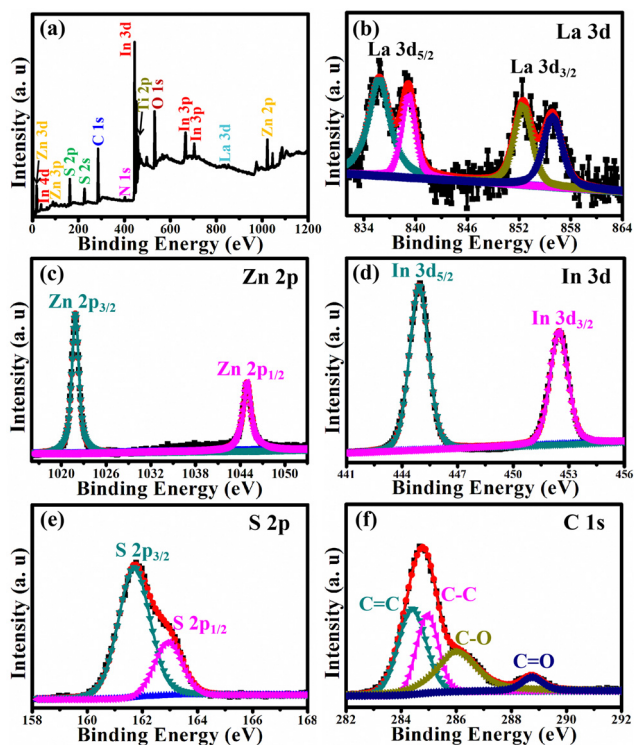**Fig. 7** The XPS spectra of La-$ZnIn_2S_4$/MIL-125(Ti) with (a) survey spectrum, (b) La 3d, (c) Zn 2p, (d) In 3d, (e) S 2p, and (f) C 1s.
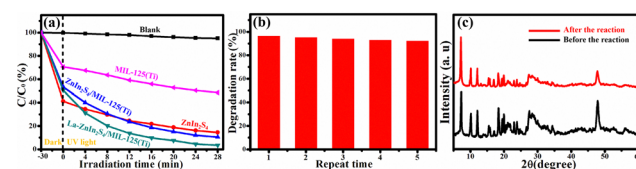

Fig. 8 (a) Photocatalytic degradation of AFB_1 by different catalysts; (b) five repetitive cycles for the photocatalytic degradation of AFB_1 by La-$ZnIn_2S_4$/MIL-125(Ti); and (c) XRD patterns of La-$ZnIn_2S_4$/MIL-125(Ti) before and after the reaction.
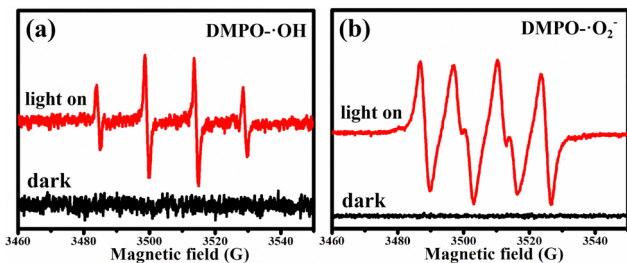
Fig. 9 ESR spectra of (a) DMPO-$^{\bullet}$OH and (b) DMPO-$^{\bullet}$O$_2^-$ for La-ZnIn$_2$S$_4$/MIL-125(Ti).

indicating that both $^{\bullet}$O$_2^-$ and $^{\bullet}$OH are generated by La-ZnIn$_2$S$_4$/MIL-125(Ti) during the photocatalysis.

The photocatalysis performance of ZnIn$_2$S$_4$ was improved by the doping of La and the coupling of MIL-125(Ti), with improved charge separation. Herein, the enhanced photocatalytic performance of AFB$_1$ degradation on the La-ZnIn$_2$S$_4$/MIL-125(Ti) photocatalyst with UV excitation is explored, and the possible schematic diagram is shown in Fig. 10. With UV illumination, valence electrons in ZnIn$_2$S$_4$ are excited to the conduction band. The excited electrons are easily moved to La and MIL-125(Ti), resulting in an effective charge separation. Then, the photoinduced electron can combine with O$_2$ to form $^{\bullet}$O$_2^-$ and the photoinduced hole can capture the electron from OH$^-$ to generate $^{\bullet}$OH. These generated $^{\bullet}$O$_2^-$ and $^{\bullet}$OH have high oxidation. AFB$_1$ can be oxidized by superoxide radicals ($^{\bullet}$O$_2^-$ and $^{\bullet}$OH). Furthermore, MIL-125(Ti) and ZnIn$_2$S$_4$ exhibit excellent adsorption properties for AFB$_1$. They can adsorb AFB$_1$ molecules on their surface or/and in their pores to form a layer of high concentration AFB$_1$ molecules. It is also beneficial for superoxide radicals ($^{\bullet}$O$_2^-$ and $^{\bullet}$OH) to degrade AFB$_1$ molecules. The elementary reaction equations are shown as follows:
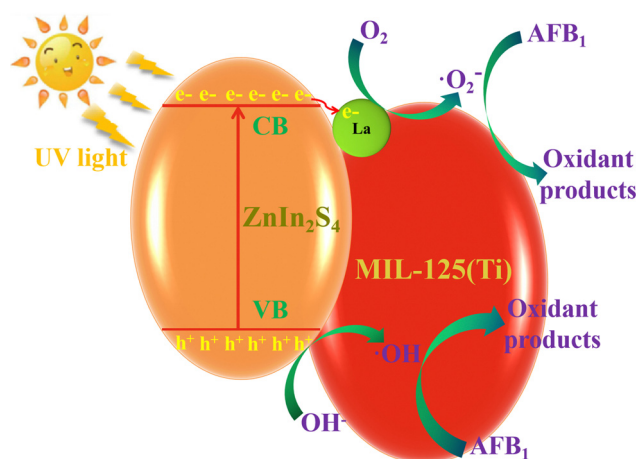
$$\text{La-ZnIn}_2\text{S}_4\text{/MIL-125(Ti)} + \text{AFB}_1 \; \text{MIL-125(Ti}_2\text{S}_4\text{/MIL-125(Ti)} + \text{AFB}_1)_{\text{adsorption}} \quad (1)$$

$$\text{La-ZnIn}_2\text{S}_4\text{/MIL-125(Ti)} + h\nu \rightarrow \text{La-ZnIn}_2\text{S}_4\text{/MIL-125(Ti)}(e^-/h^+)$$
$$\rightarrow (e^- + h^+) \quad (2)$$

$$e^- + O_2 + {}^{\bullet}O_2^- \quad (3)$$

$$e^- + OH^- + {}^{\bullet}OH \quad (4)$$

$${}^{\bullet}O_2^- + (\text{La-ZnIn}_2\text{S}_4\text{/MIL-125(Ti)} + \text{AFB}_1)_{\text{adsorption}}$$
$$\text{dsoxidant products} \quad (5)$$

$${}^{\bullet}OH + (\text{La-ZnIn}_2\text{S}_4\text{/MIL-125(Ti)} + \text{AFB}_1)_{\text{adsorption}}$$
$$\text{dsoxidant products} \quad (6)$$

where (La-ZnIn$_2$S$_4$/MIL-125(Ti) + AFB$_1$)$_{\text{adsorption}}$ represents the AFB$_1$ molecules adsorbed on the surface or/and in the pores of La-ZnIn$_2$S$_4$/MIL-125(Ti).

Conclusions

In conclusion, we successfully fabricated the La doped ZnIn$_2$S$_4$/MIL-125(Ti) composite *via* a solvothermal method, which exhibits the best photocatalytic performance in the AFB$_1$ degradation with UV excitation. After 28 min of UV light irradiation, La-ZnIn$_2$S$_4$/MIL-125(Ti) can degrade 97.6% of AFB$_1$, the highest among all samples. It was demonstrated that the doping of La and the coupling with MIL-125(Ti) could narrow the band gap energy, improve the BET surface area and enhance the charge separation and electron transfer of ZnIn$_2$S$_4$, resulting in the drastic enhancement of photocatalysis. The electron spin resonance (ESR) technique also verified that $^{\bullet}$OH and $^{\bullet}$O$_2^-$ are the reactive radicals for the decomposition of AFB$_1$ during the photodegradation process. This study provided a novel strategy to fabricate semiconductor-based photocatalysts with enhanced photocatalytic performance to eliminate and prevent the AFB$_1$ contamination in the food security areas.

Author contributions

Xiaobing Yang: formal analysis, preparation and characterization of the samples, and writing – original draft preparation. Junjie Pan, Bingcong Xing and Wenjie Lei: preparation and characterization of the samples and carrying out the photocatalytic degradation testing. Yingchun Fu and Kejun Cheng: providing the idea of this work and designing relevant experiments, writing – review and editing, and funding acquisition.

Conflicts of interest

There are no conflicts to declare.

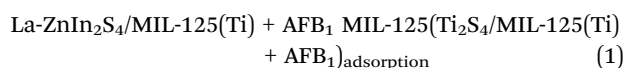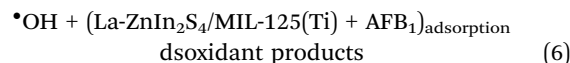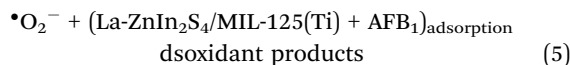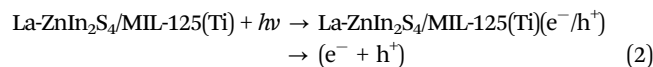## Acknowledgements

Fig. 10 Illustration of the photocatalytic mechanism of AFB$_1$ degradation on the La-ZnIn$_2$S$_4$/MIL-125(Ti) photocatalyst under UV light irradiation.

Notes and references

1 M. S. Samuel, K. Mohanraj, N. Chandrasekar, R. Balaji and E. Selvarajan, Synthesis of recyclable $GO/Cu_3(BTC)_2/Fe_3O_4$ hybrid nanocomposites with enhanced photocatalytic degradation of aflatoxin B1, *Chemosphere*, 2022, **291**, 132684.

2 O. A. Adebo, P. B. Njobeh and V. Mavumengwana, Degradation and detoxification of AFB_1 by Staphylococcus warneri, Sporosarcina sp. and Lysinibacillus fusiformis, *Food Control*, 2016, **68**, 92–96.

3 P. B. Mathur, S. Sunkara, M. B. Panwar, F. Waliyar and F. W. K. K. Sharma, Biotechnological advances for combating Aspergillus flavus and aflatoxin contamination in crops, *Plant Sci.*, 2015, **234**, 119–132.

4 S. Marin, A. J. Ramos, G. C. Sancho and V. Sanchis, Mycotoxins: occurrence, toxicology, and exposure assessment, *Food Chem. Toxicol.*, 2013, **60**, 218–237.

5 L. Mao, H. Liu, L. Yao, W. Wen, M. M. Chen, X. Zhang and S. Wang, Construction of a dual-functional CuO/BiOCl heterojunction for high-efficiently photoelectrochemical biosensing and photoelectrocatalytic degradation of aflatoxin B1, *Chem. Eng. J.*, 2022, **429**, 132297.

6 H. Xu, J. Sun, H. Wang, Y. Zhang and X. Sun, Adsorption of aflatoxins and ochratoxins in edible vegetable oils with dopamine-coated magnetic multi-walled carbon nanotubes, *Food Chem.*, 2021, **365**, 130409.

7 H. Rastegar, S. Shoeibi, H. Yazdanpanah, M. Amirahmadi, A. M. Khaneghah, F. B. Campagnollo and A. S. Sant'Ana, Removal of aflatoxin B_1 by roasting with lemon juice and/or citric acid in contaminated pistachio nuts, *Food Control*, 2017, **71**, 279–284.

8 F. Xing, L. Wang, X. Liu, J. N. Selvaraj, Y. Wang, Y. Zhao and Y. Liu, Aflatoxin B1 inhibition in Aspergillus flavus by Aspergillus niger through downregulating expression of major biosynthetic genes and AFB1 degradation by atoxigenic A. flavus, *Int. J. Food Microbiol.*, 2017, **256**, 1–10.

9 P. Yang, S. Lu, W. Xiao, Z. Zheng, S. Jiang, S. Jiang, S. Jiang, J. Cheng and D. Zhang, Activity enhancement of Trametes versicoloraflatoxin B1-degrading enzyme (TV-AFB1D) by molecular docking and site-directed mutagenesis techniques, *Food Bioprod. Process.*, 2021, **129**, 168–175.

10 P. Udomkun, A. N. Wiredu, M. Nagle, J. Müller, B. Vanlauwe and R. Bandyopadhyay, Innovative technologies to manage aflatoxins in foods and feeds and the profitability of application-A review, *Food Control*, 2017, **76**, 127–138.

11 D. S. Bhatkhande, V. G. Pangarkar and A. A. C. M. Beenackers, Photocatalytic degradation for environmental applications-a review, *J. Chem. Technol. Biotechnol.*, 2002, **77**, 102–116.

12 Y. Kumar, P. Kumar, P. Raizada, A. A. P. Khan, Q. V. Le, P. Singh and V. H. Nguyen, Novel Z-Scheme $ZnIn_2S_4$-based photocatalysts for solar-driven environmental and energy applications: Progress and perspectives, *J. Mater. Sci. Technol.*, 2021, **87**, 234–257.

13 W. Jiang, Z. Li, C. Liu, D. Wang, G. Yan, B. Liu and G. Che, Enhanced visible-light-induced photocatalytic degradation of tetracycline using BiOI/MIL-125(Ti) composite photocatalyst, *J. Alloys Compd.*, 2021, **854**, 157166.

14 F. Mu, Q. Cai, H. Hu, J. Wang, Y. Wang, S. Zhou and Y. Kong, Construction of 3D hierarchical microarchitectures of Z-scheme $UiO-66-(COOH)_2/ZnIn_2S_4$ hybrid decorated with non-noble MoS_2 cocatalyst: A highly efficient photocatalyst for hydrogen evolution and Cr(VI) reduction, *Chem. Eng. J.*, 2020, **384**, 123352.

15 X. Yuan, H. Wang, Y. Wu, G. Zeng, X. Chen, L. Leng, Z. Wu and H. Li, One-pot self-assembly and photoreductionsynthesis of silver nanoparticle-decoratedreduced graphene oxide/MIL-125(Ti) photocatalyst with improved visible light photocatalytic activity, *Appl. Organomet. Chem.*, 2016, **30**, 289–296.

16 H. Wang, X. Yuan, Y. Wu, G. Zeng, H. Dong, X. Chen, L. Leng, Z. Wu and L. Peng, In situ synthesis of In_2S_3@MIL-125(Ti) core-shell microparticle for the removal of tetracycline from wastewater by integrated adsorption and visible-light-driven photocatalysis, *Appl. Catal., B*, 2016, **186**, 19–29.

17 S. Mao, J. W. Shi, G. Sun, D. Ma, C. He, Z. Pu, K. Song and Y. Cheng, Au nanodots@thiol-UiO66@$ZnIn_2S_4$ nanosheets with significantly enhanced visible-light photocatalytic H_2 evolution: The effect of different Au positions on the transfer of electron-hole pairs, *Appl. Catal., B*, 2021, **282**, 119550.

18 M. Cao, F. Yang, Q. Zhang, J. Zhang, L. Zhang, L. Li, X. Wang and W. L. Dai, Facile construction of highly efficient MOF-based $Pd@UiO-66-NH_2@ZnIn_2S_4$ flower-like nanocomposites for visible-light-driven photocatalytic hydrogen production, *J. Mater. Sci. Technol.*, 2021, **76**, 189–199.

19 B. Gao, L. F. Liu, J. D. Liu and F. L. Yang, Photocatalytic degradation of 2,4,6-tribromophenol over Fe-doped $ZnIn_2S_4$: Stable activity and enhanced debromination, *Appl. Catal., B*, 2013, **129**, 89–97.

20 Q. Zhu, Y. Sun, S. Xu, Y. Li, X. Lin and Y. Qin, Rational design of 3D/2D In_2O_3 nanocube/$ZnIn_2S_4$ nanosheet heterojunction photocatalyst with large-area "high-speed channels" for photocatalytic oxidation of 2,4-dichlorophenol under visible light, *J. Hazard. Mater.*, 2020, **382**, 121098.

21 J. Ding, Z. Q. Yang, C. He, X. W. Tong, Y. Li, X. J. Niu and H. G. Zhang, UiO-66(Zr) coupled with Bi_2MoO_6 as photocatalyst for visible-light promoted dye degradation, *J. Colloid Interface Sci.*, 2017, **497**, 126–133.

22 H. Fakhri, M. Farzadkia, V. Srivastava and M. Sillanpää, Designed synthesis of perylene diimide-based supramolecular heterojunction with g-C_3N_4@MIL-125(Ti): insight into photocatalytic performance and mechanism, *J. Mater. Sci.: Mater. Electron.*, 2021, **32**, 19–32.

23 S. Yin, Y. Chen, C. Gao, Q. Hu, M. Li, Y. Ding, J. Di, J. Xia and H. Li, In-situ preparation of MIL-125(Ti)/Bi_2WO_6 photocatalyst with accelerating charge carriers for the photodegradation of tetracycline hydrochloride, *J. Photochem. Photobiol., A*, 2020, **387**, 112149.

24 R. Yuan, J. Qiu, C. Yue, C. Shen, D. Li, C. Zhu, F. Liu and A. Li, Self-assembled hierarchical and bifunctional MIL-88A(Fe)@$ZnIn_2S_4$ heterostructure as a reusable sunlight-driven photocatalyst for

highly efficient water purification, *Chem. Eng. J.*, 2020, **401**, 126020.

25 Z. Zhang, L. Huang, J. Zhang, F. Wang, Y. Xie, X. Shang, Y. Gu, H. Zhao and X. Wang, In situ constructing interfacial contact $MoS_2/ZnIn_2S_4$ heterostructure for enhancing solar photocatalytic hydrogen evolution, *Appl. Catal., B*, 2018, **233**, 112–119.

26 Y. Zhao, Y. Chen, L. Du, Q. Wang, X. Liu, L. Li and G. Tian, Fabrication of size-controlled hierarchical $ZnS@ZnIn_2S_4$ heterostructured cages for enhanced gas-phase CO_2 photoreduction, *J. Colloid Interface Sci.*, 2022, **605**, 253–262.

27 X. B. Yang, Z. Yang, S. Zhao, J. Hu and X. Luo, Synthesis of mesoporous Si/SiC with three-dimensional structure derived from C/silicalite-1 via magnesiothermic reduction, *J. Porous Mater.*, 2018, **25**, 713–717.

28 J. J. Ding, W. H. Yan, S. Sun, J. Bao and C. Gao, Hydrothermal synthesis of $CaIn_2S_4$-reduced graphene oxide, nanocomposites with increased photocatalytic performance, *ACS Appl. Mater. Interfaces*, 2014, **6**, 12877–12884.

29 R. Shwetharani, A. Poojashree, R. B. Geetha and M. S. Jyothi, La activated high surface area titania float for the adsorption of Pb(ii) from aqueous media, *New J. Chem.*, 2018, **42**, 1067–1077.

30 T. Jia, W. Wang, F. Long, Z. Fu, H. Wang and Q. Zhang, Fabrication, characterization and photocatalytic activity of La-doped ZnO nanowires, *J. Alloys Compd.*, 2009, **484**, 410–415.